Materialia 26 (2022) 101614

Contents lists available at ScienceDirect

Materialia

journal homepage: www.elsevier.com/locate/mtla

On the relationship between laser scan strategy, texture variations and hidden nucleation sites for failure in laser powder-bed fusion

Victor Pacheco[a], Jithin James Marattukalam[b], Dennis Karlsson[a], Luc Dessieux[c], Khanh Van Tran[d], Premysl Beran[e], Ingo Manke[d], Nikolay Kardjilov[d], Henning Markötter[d,f], Martin Sahlberg[a], Robin Woracek[e,*]

[a] Department of Chemistry - Ångström Laboratory, Uppsala University, Box 523, SE-75120 Uppsala, Sweden
[b] Department of Physics, Materials Physics, Uppsala University, Box 530, SE-75121 Uppsala, Sweden
[c] Oak Ridge National Laboratory, Oak Ridge, Tennessee 37831, USA
[d] Helmholtz-Zentrum Berlin für Materialien und Energie (HZB), Hahn-Meitner-Platz 1, 14109 Berlin, Germany
[e] European Spallation Source ERIC, Box 176, 22100 Lund, Sweden Nuclear Physics Institute, Czech Academy of Sciences, 250 68, Řež, Czech Republic
[f] Bundesanstalt für Materialforschung und -Prüfung (BAM), Unter den Eichen 87, 12205 Berlin, Germany

ARTICLE INFO

Keywords:
Laser powder-bed fusion
Texture
Preferential orientation
Diffraction contrast neutron imaging
Bragg-edge
Inhomogeneous microstructure
Texture control

ABSTRACT

While laser powder-bed fusion has overcome some of the design constraints of conventional manufacturing methods, it requires careful selection of process parameters and scan strategies to obtain favorable properties. Here we show that even simple scan strategies, complex ones being inevitable when printing intricate designs, can inadvertently produce local alterations of the microstructure and preferential grain orientation over small areas – which easily remain unnoticed across the macroscale. We describe how a combined usage of neutron imaging and electron backscatter diffraction can reveal these localized variations and explain their origin within cm-sized parts. We explain the observed contrast variations by linking the neutron images to simulated data, pole figures and EBSD, providing an invaluable reference for future studies and showing that presumably minor changes of the scan strategy can have detrimental effects on the mechanical properties. In-situ tensile tests reveal that fracture occurs in a region that was re-melted during the building process.

1. Introduction

In the manufacturing industry, a common experience for designers and engineers, is that the complex geometries and designs that they conceive cannot be realized in practice due to limitations in the manufacturing techniques at their disposal. Additive manufacturing (AM) or 3D printing is a group of novel techniques that can overcome the design constraints of conventional methods [1–3]. Among metal AM techniques, laser powder-bed fusion (LPBF) is the most widely used method [4–6]. In LPBF, a laser is used to selectively melt areas of a powder-bed according to a digital model. New layers of powder are subsequently added and the process is repeated until the component is completed [7,8].

Besides the advantages of LPBF for the creation of complex designs, its distinctive solidification conditions (high cooling rates and thermal gradients) [9–11] offer unique possibilities for the development of materials with tailored microstructures and properties. This can be exploited for instance to produce non-equilibrium phases, such as amorphous metals, [12–15] to tailor the preferential orientation of grains [16] (also known as texture) and even to produce complex microstructures that resemble ancient Damascus steel [17]. Texture and microstructure control are especially relevant, as they can be used as additional design tools, capable of tuning and enhancing material properties and performance in ferromagnetic materials [18], as well as in structural parts [19].

In recent years tremendous progress has been made in understanding the microstructure and texture formation mechanism that takes place in LPBF [9,16,20]. Although the laser path and heat transfer have been shown to play a central role, [21,22] the local microstructural variations that could be produced by some commonly used laser scan strategies, such as chess, stripes with shift, and islands with shift, have not been properly investigated across cm-length scales. Even though local microstructural variations could affect the mechanical and functional properties of a material, the topic has been largely overlooked. Understanding the effect of the scan strategy on the local microstructure and texture development is especially relevant to produce intricate components, which often require complex scan strategies. In this study, texture differences between 316L stainless steel components that were produced with different – relatively simple – scan strategies are visualized and characterized. More importantly, we reveal localized microstructure and

* Corresponding author.
E-mail address: robin.woracek@ess.eu (R. Woracek).

https://doi.org/10.1016/j.mtla.2022.101614
Received 19 July 2022; Accepted 28 October 2022
Available online 29 October 2022

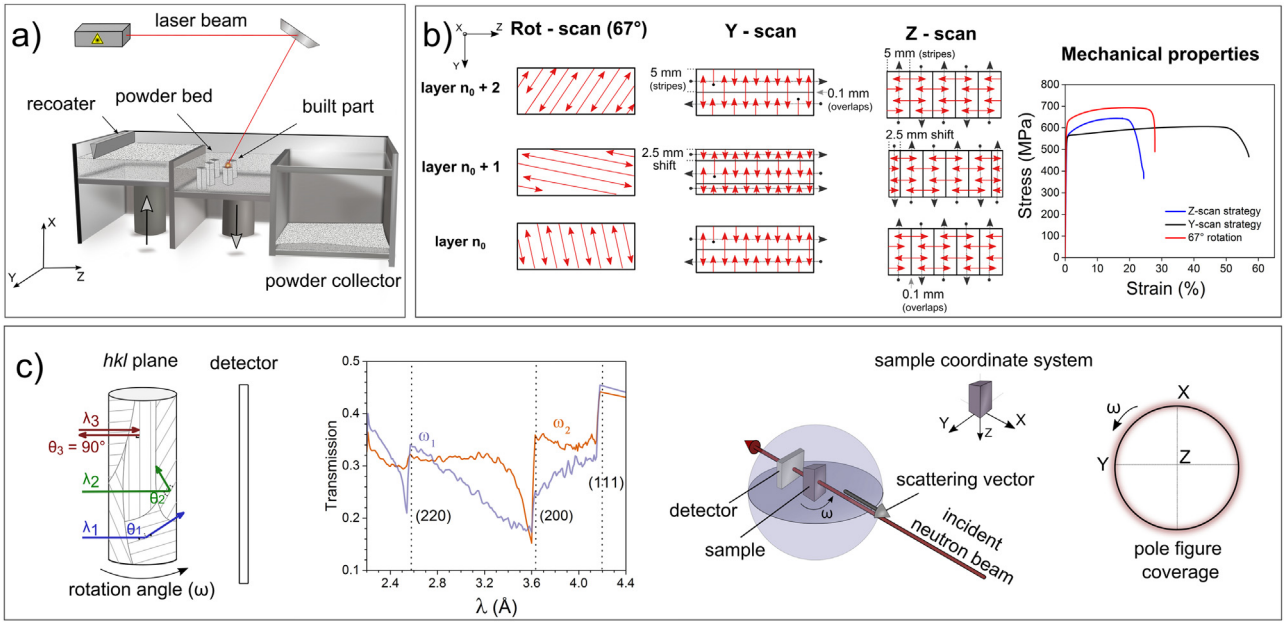

Fig. 1. a) Basic setup and components of the laser powder-bed fusion (LPBF) process. b) The three laser scan strategies used for the production of the 316L stainless steel samples and their mechanical properties. Mechanical properties are from previous work by Marattukalam et al.[16]. The path of the laser beam is indicated with red arrows and black arrows are used to show the scanning order. Note that subsequent layers are 'shifted' compared to the previous layer. c) The principle of diffraction contrast neutron imaging. Transmission spectra are shown for face centered cubic iron, where preferred grain orientation (texture) leads to distinct spectral differences as a function of sample orientation ω. The imaging geometry, with the relevant scattering vector corresponding to a Bragg edge is illustrated. A red circle indicates the resultant pole figure coverage when rotating a sample by ω=360°.

texture alterations within the same samples and establish a connection to the scanning strategy. This was only possible by employing diffraction contrast neutron imaging and we herein provide a comprehensive interpretation of the imaging data, which elucidates the relation between the laser movement and the local texture and microstructure evolution during the LPBF process. Moreover, we show, by in-situ tensile testing, that the local alterations have a notable effect on the failure mechanism.

2. Materials and methods

2.1. Laser powder-bed fusion

The samples used in this study were produced using an EOSM100 printer (Yb fiber laser, spot size of 40 μm) with gas atomized 316L stainless steel powders provided by EOS GmbH. The D10, D50 and D90 (i.e., particle diameter that corresponds to each cumulative percentage in the particle size distribution) values of the powder are 20 μm, 40 μm, and 60 μm, respectively. The LPBF parameters were previously optimized [16] to obtain dense, crack-free samples and the final samples were manufactured using a laser power of 107 W, scan speed of 827 mm/s, 70 μm hatch distance, stripe width of 5 mm, 100 μm in the overlap between the stripes and 20 μm layer thickness. More details are provided elsewhere [16]. Three different bi-directional scan strategies, namely, 67° rotation scans, Y-scan and Z-scan were implemented, as illustrated in Fig. 1.

The motivation to use these three scan strategies in this work are multifold: (i) they have been previously shown to produce different type of crystallographic texture, which in turn leads to significant differences of the mechanical properties [16]. (ii) The possibility to locally tailor crystallographic anisotropic texture and microstructure with these types of scan strategies provides a tool to influence and enhance material properties in additive manufacturing. Eventually this may allow for "anisotropic property development" in a three-dimensional body. And while the latter may require more complex scan strategies than the ones chosen, one needs to first establish a thorough understanding of the microstructure development which can only be obtained by (iii) relatively simple scan strategies. In this case, a similar scan pattern with only slight variations repeats throughout the build direction, which enables the investigation of their effect on the local texture variations, mechanical properties, and failure of the evaluated specimens by means of neutron radiography and EBSD. The three scan strategies were employed to manufacture rectangular samples of 60 × 10 × 10 mm, as shown in Fig. S1 of the SI.

2.2. Diffraction contrast neutron imaging

The diffraction contrast neutron imaging measurements were conducted at the CONRAD-2 beamline in Helmholtz-Zentrum Berlin (HZB). Radiographic images were taken at distinct wavelengths between 2.2 and 4.6 Å in constant steps of 0.02 Å (121 in total), using a tunable double crystal monochromator ($\Delta\lambda/\lambda \approx 3\%$) [23].

This wavelength range was chosen as it covers the most prominent Bragg edges and extends beyond the Bragg cut-off, i.e. the wavelengths where no more Bragg scattering takes place (compare Fig. 2c). The images (each with 180 s exposure) were normalized by removing the detector offset with the subtraction of the dark field image (without neutron beam) and dividing by an open beam scan (with neutron beam and without sample). For the main line of investigation, three distinct wavelengths were selected (namely λ = 2.58, 3.34 and 3.8 Å) in order to investigate the lattice plane families corresponding to (220), (200) and (111), respectively. The calibration of the neutron wavelength from the double-crystal monochromator was determined by fitting Bragg edge data from standard iron powder.

2.3. In-situ tensile testing during neutron imaging

Tensile testing was carried out during in-situ neutron imaging by using a custom built loading system [24] that allows for sample rotation under the applied load. Cylindrical tensile samples were machined from the as-printed (rectangular) samples with a diameter of d = 5 mm and a gauge length of L = 15 mm. While as manufactured AM parts often

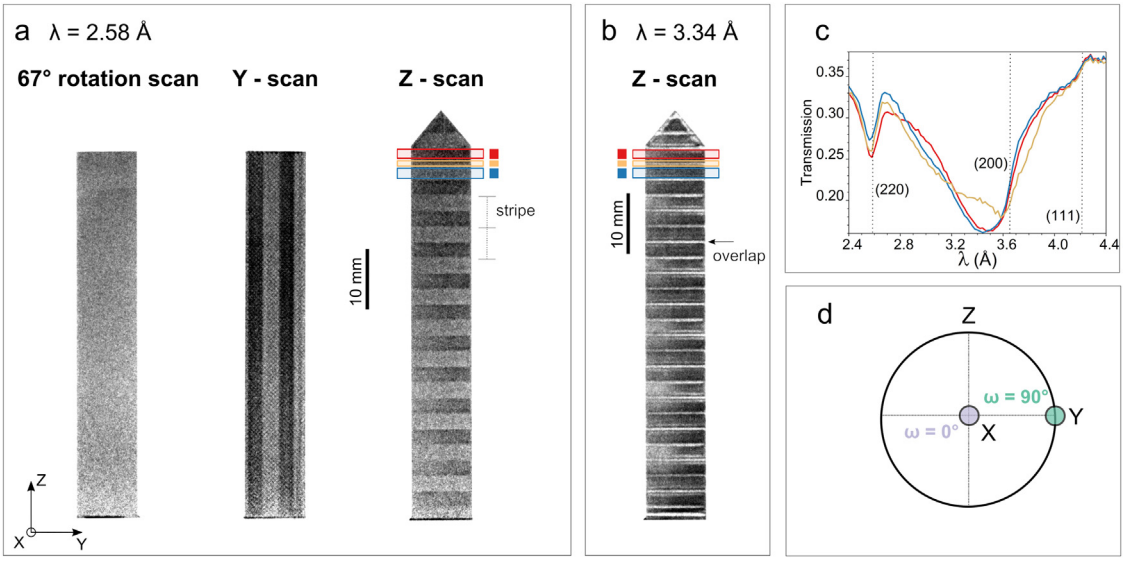

Fig. 2. a) Neutron transmission images with $\lambda = 2.58$ Å of the 316L stainless steel samples produced with 67° rotation scan, Y-scan and Z-scan strategies. The build direction in all cases is along the x-direction (corresponding to a sample rotation of $\omega = 0°$). b) Neutron transmission image with $\lambda = 3.34$ Å of the sample produced with a Z-scan strategy. c) Transmission spectra for different areas of the Z-scan sample. The expected positions of the Bragg-edges are shown with vertical lines. d) The two different orientations of the sample with respect to the neutron beam (rotation around the z-axis), are also illustrated in a model pole figure.

possess rough surfaces that can dominate the mechanical testing properties, care was taken to produce smooth surfaces by machining. Continuous loading experiments were performed with a deformation rate of 10 μm/min using a fixed neutron wavelength of 3.8 Å and 60 s exposure.

2.4. Neutron pole figures

Average pole figures of the as-printed samples were measured using neutron diffraction. The measurements were conducted on the MEREDIT instrument at the Nuclear Physics Institute, Czech Republic, with a neutron wavelength of 1.46 Å. The texture was evaluated as an average from the sample volume of 10 × 10 × 10 mm^3. An Euler goniometer allowed the rotation of the samples around the φ (0 - 360°) and χ (0 - 90°) angles, with a step size of 5°. The variation of the diffracted intensities as a function of different orientations was obtained for four reflections, namely (311), (220), (200) and (111). From this data, the orientation distribution function (ODF) was determined for each sample and the pole figures were calculated using the A-Tex software [25].

2.5. Simulation

Neutron transmission simulations were performed to characterize the texture components in the additive manufactured 316L stainless steel samples, using the Sinpol [26] application. Sinpol is a collection of sub-routines for calculation of the total cross section that determines the attenuation of the neutron beam by a crystalline specimen. The total cross section is calculated as a function of neutron wavelength, crystal structure, temperature, and crystal orientation distribution. The contribution of the coherent elastic scattering to the total cross section is evaluated within secondary extinction theory using both the crystal's mosaic spread value and its orientation with respect to the neutron beam direction. The simulation of the 316L stainless steel sample is represented with an iron plate of 10 mm, and a set of 10000 grain orientations were generated from the measured neutron pole figures, using the MTEX software [27]. The main physical parameters required for the neutron transmission simulations, namely atomic mass, unit cell parameter, Debye temperature (Θ_D), the neutron coherent scattering length (b), the total bound scattering cross section (σ_b) and the neutron absorption cross section (σ_{abs}) are obtained from literature [28–31] and the neutron diffraction measurements that are listed in table S1 of the SI.

2.6. Electron backscatter diffraction

The electron backscatter diffraction experiments were conducted using a Zeiss Merlin FEG scanning electron microscope (SEM), equipped with a Nordlys Max detector for acquiring EBSD patterns. The SEM was operating at an acceleration voltage of 20 kV and a beam current of 10 nA at a working distance of 14 mm. Large maps were constructed by acquiring multiple maps at 500 x magnification and stitching them together using the AZtec HKL software by Oxford instruments. The pole figures were constructed from selected regions using the HKL Channel 5 software. Prior to the EBSD measurements the samples were sequentially polished using diamond suspensions with particle sizes of 9 µm, 3 µm and 1 µm. The final surface finish was obtained by a 40 nm colloidal silica polishing step.

3. Results

3.1. Effect of the laser scan strategy on the local microstructure and texture

We recently showed [16] that three distinct laser scan strategies (see Fig. 1a-b) for the manufacture of 316L stainless steel samples resulted in different types of preferential orientation of the grains, which in turn leads to significant differences of the mechanical properties. The three scan strategies are referred to as 67° rotation-, Y- and Z-scan and are illustrated in Fig. 1b. The samples produced with these scan strategies were characterized in the present work, using primarily diffraction contrast neutron imaging. The method exploits the fact that Bragg scattering is a strong contributor to the attenuation of the neutron beam for many polycrystalline materials, resulting in a transmission pattern that is characteristic for their crystalline structure.

The principle behind diffraction contrast in neutron imaging is illustrated in Fig. 1c for a specific *hkl* plane family. As depicted, the scattering angle increases with increasing wavelengths until a maximum value is obtained at the wavelength $\lambda_3 = 2d_{hkl}$, where d_{hkl} is the *hkl* interplanar spacing. At this wavelength, the diffraction angle 2θ is 180° (backscattering); and for any larger wavelengths, Bragg's law cannot be satisfied

any longer for the corresponding plane family. The sharp increases in the transmission spectra are refereed to as Bragg-edges. Two simulated transmission spectra for a textured polycrystalline face center cubic (fcc) iron are also illustrated in Fig. 1c, to highlight the dependency on sample orientation. A strongly pronounced Bragg-edge corresponds to many grains being aligned for backscattering condition, i.e. the plane normals are parallel to the incident beam direction. Accordingly, by recording neutron transmission as a function of wavelength and sample orientation, it is possible to obtain information about grain orientations in polycrystalline samples. Fig. S2 depicts a simulated transmission map for the textured polycrystalline fcc iron, showing the variations with wavelength (λ) and sample rotation around the vertical axis (ω). The imaging geometry, with the corresponding scattering vector for Bragg-edge analysis, is also illustrated in Fig. 1c. This experimental set-up allows to probe the outer circumference of the pole figure (the most common tool used to describe texture) by rotating the sample around ω.

The diffraction contrast neutron imaging experiments resulted in series of transmission images at different neutron wavelengths. Images obtained with a wavelength of 2.58 Å are shown in Fig. 2a. The experimental set-up and arrangement of the samples is shown in Fig. S1 of the SI. An animated sequence of the images collected with the different wavelengths used in this study (2.2 to 4.6 Å with 0.02 Å steps) can be found in the SI.

As illustrated in Fig. 2a, the sample fabricated with the 67° rotation scan, does not show any significant contrast variations, whereas some sections of samples Y and Z do. In the case of sample Z, a periodic change of contrast is revealed along the z-axis, with alternating dark and bright bands appearing. The length of these bands is approximately 2.5 mm, which corresponds to half of the stripe length used to produce the samples (see Fig. 1b). A similar pattern, with bands of 2.5 mm in length, can be seen in sample Y, with the variations along the y-axis. The presence of the bands that are visible in Fig. 2a was unforeseen, as the laser parameters and scan strategies employed for sample Y and Z were expected to produce textured samples without significant local variations. Samples produced with the Y- and Z-scan strategies were found to have a texture component that resembles a single crystal – with <110> parallel to the build direction and <100> oriented in the direction of the laser movement – by neutron pole figures and EBSD in our previous study [14]. On the other hand, a fiber texture was observed in samples produced with 67° rotation of the scan vectors [14]. Local variations of texture or microstructure were not identified, as neutron pole figures only provided an average description of the texture component, without spatially resolved information and EBSD probed the material at length scales that were too small to reveal the differences seen in Fig. 2a. These images already highlight the importance of such additional full-field characterization to evaluate manufactured components across the mm- and cm-length scales with spatially resolved information. Here is it also relevant to mention that recently, some variations of crystallographic texture have been observed in 316L parts produced by LPBF with the use of diffraction contrast neutron imaging [32]. The variations seen in that study were mostly confined to the edges of the samples and do not resemble the results seen in Fig. 2a. The origin of those variations was not clearly elucidated, but the processing parameters, scan strategies and/or defects were pointed out as possible causes for the changes near the surface.

The interpretation of contrast variations in diffraction contrast neutron imaging can be complex, as many factors can contribute to the observed differences [32,33]. We will show and discuss in the following sections that the contrast variations between the bands can be attributed to changes in the preferential orientation of the grains. For instance, the images in Fig. 2a were recorded at a wavelength of 2.58 Å and a Bragg-edge originating from the (220) family of planes is expected around 2.6 Å for fcc iron. Hence, a stronger attenuation (darker gray value) indicates that more grains are aligned with the (220) plane normals parallel to the direction of the incident neutron beam, i.e. causing more neutrons to be diffracted out of the incident path, at an angle close to $2\theta = 180°$.

The images collected with a neutron wavelength of 3.34 Å do not show the same bright and dark bands, but they reveal additional inhomogeneities in sample Y and Z, while the sample produced using 67° rotation does not show any significant contrast variations. These inhomogeneities can be seen in Fig. 2b for sample Z and although the underlying mechanism for their formation is not clear at the moment, their periodic appearance along the Z-axis (repeating at every fourth visible horizontal 'band') suggest that they are related to flaws generated during the manufacturing process. The images of the samples fabricated with the 67° rotation and Y-scan strategies can be found in Fig. S3 of the SI. The periodic bright lines seen every 2.5 mm, correspond to the 0.1 mm overlaps used in the manufacturing of the specimens (stripe overlaps, see Fig. 1b). The strength of wavelength selective neutron radiography is apparent here as it reveals otherwise hidden or overlooked inhomogeneities.

The *hkl* plane family that is particularly probed with a wavelength of 3.34 Å corresponds to (200), where a Bragg-edge is expected at 3.65 Å for fcc iron – note that (111) still contributes to Bragg scattering at this wavelength. From Fig. 2b, it can be seen that the overlaps have a different average distribution of the <100> directions in comparison to other sections of the sample, thereby causing more transmission at this wavelength (and corresponding diffraction angle). These lines could not be observed after a 90° rotation of the sample, which indicates a strong degree of anisotropy in these areas.

To gain a better understanding of the variations seen in Fig. 2a and 2b, the transmission spectra of different sections of sample Z were obtained, as shown in Fig. 2c. For the (220) planes, the lowest transmission is obtained in the dark band regions (red line), while the region corresponding to the stripe overlap (yellow line) displays a transmission between the bright and dark bands. The exact mechanism causing the contrast differences between the observed bands will be discussed in combination with the EBSD results.

To explain the presence of the distinct bands observed in Fig. 2a, their origin was investigated through inspection of the laser movement (scan vectors and scanning order). During the manufacturing process, a 2.5 mm shift of the stripes was used between each layer, as illustrated in Fig. 3. This shift produces an effective alternation of laser movement and laser scanning order along the build direction inside each observed band, resulting in four distinct combinations.

The laser movement (laser scan vectors) was alternating in what is observed as bright bands (every second layer), while the same path was taken in what is observed as dark bands (across all the layers). The scanning order also alternates, resulting in the bright bands being built using the same scanning order and the dark bands being built by opposed scanning orders at every second layer.

3.2. Transmission spectra (experiment and simulations)

The transmission spectra obtained at different orientations can provide a description of the type of texture present in a component and its strength (as previously shown in Fig. 1c). Consequently, the transmission spectra were evaluated for the three types of samples used in this study, at two orthogonal orientations ($\omega = 0°$ and 90°), as can be seen in Fig. 4. The transmission spectra were obtained from relatively large areas (as shown in Fig. S4 of the SI), so as to obtain an average description of the samples, corresponding to a volume that was probed neutron diffraction to obtain the pole figures. In order to further demonstrate that the transmission plots provide a good description of the texture characteristics of the parts, transmission spectra were simulated for each sample, based on the experimental neutron pole figures measured in our previous work [16]. The neutron transmission simulation spectra of each sample was calculated in two steps: first, each associated experimental pole figure is converted into an ODF using MTEX [27] (the ODF consist a three dimensional array of Euler angles), second, the transmission spectra is calculated by inserting the ODF into the SINPOL [26] simula-

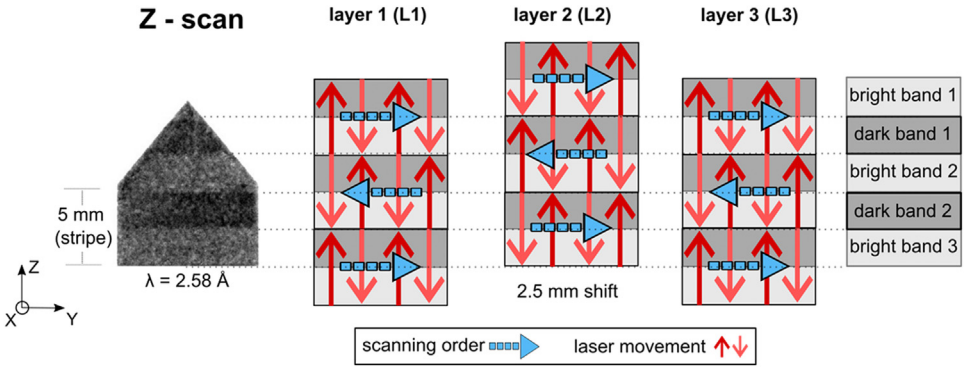

Fig. 3. The bright and dark bands seen by neutron radiography in the Z-scan samples and an illustration of the corresponding scanning order direction (blue) and laser movement direction (red) are shown. Note that layer 1 and layer 3 are identical. There are four distinct combinations of scanning order and laser movement between layer 1 and layer 2 (with bright band 3 being equal to bright band 1). The build direction is along the x-direction (corresponding to a sample rotation of $\omega = 0°$).

tion tools, this approach is consistent with previous texture calculations [29] employing SINPOL.

These experimental pole figures are shown in Fig. 4a. The experimental spectra (black lines) show a good agreement with the simulated ones (red lines), as observed in Fig. 4b and 4d.

In Fig. 4d it can be seen that for an orientation of $\omega = 0°$ (build direction parallel to the neutron beam), all three types of samples exhibit pronounced Bragg-edges for the (220) plane, indicating a strong parallel alignment of the ⟨110⟩ directions to the build direction. Therefore, the spectra confirm the parallel alignment of the ⟨110⟩ directions to the build direction seen in the pole figures of Fig. 4a. For comparison, the (220) Bragg-edge is much less pronounced at $\omega = 90°$ for the Y-scan, as seen in Fig. 4b, which agrees with no visible intensity in the (110) pole figure depicted in Fig. 4a.

Fig. 4c shows the simulated transmission maps, which summarize the variation of transmitted intensity with sample rotation and wavelength, while experimentally only two orthogonal orientations were evaluated. An important implication of the results summarized in Fig. 4 is that a good picture of the type of texture in a component can often be obtained from the neutron Bragg-edge imaging measurements, without being necessary to record complete pole figures directly. The bright and dark bands are not considered in this simulation, as these differences can later be explained by pole figures obtained by EBSD (from a smaller area).

3.3. Origin of the local microstructure and texture variations

The contrast variations observed between the different samples could be explained well with the help of the neutron pole figures and simulations. Meanwhile, the origin of the local contrast variation within the same sample(s) can be linked to the laser scan strategy, but the exact mechanism could not yet be explained. The neutron transmission spectra themselves are not conclusive but indicate that the type of texture is not significantly different in the identified sections (see Fig. 2c). Therefore, we have employed EBSD to further investigate the two main sections that can be observed in sample Z, namely the bright and dark bands. Fig. 5 shows the grain orientation map and the corresponding pole figures for the different regions discovered by neutron imaging.

In Fig. 5, it can be observed that the preferred grain orientation within the bright bands is slightly rotated in comparison to the dark bands. This is most obvious for the (110) pole figures, where a rotation around the z-axis is seen between bright band 1 and bright band 2. This misorientation in relation to the build direction/x-axis (~ 15°) indicates a tilting of the grains away from the build direction. Therefore, the previously identified bright and dark band contrast that is revealed at 2.58 Å (Fig. 2 and 3) can be attributed to tilting of the grains in the bright sections. An additional observation that is noteworthy is the variations of sharpness in the poles, with the bright bands displaying concentrated and sharp intensities, while the dark bands show a spread intensity over larger areas.

The tilting of the grains seems to be correlated with the direction of the scanning order, as the effect is only seen along the y-axis (rotation around the z-axis). One possible explanation is that part of the heat transfer occurs through a band heat transfer mechanism across the stripes, as has been previously proposed by Carter et al. [34]. This type of heat transfer mode, in combination with the uni-directional scanning order seen in the bright bands, could produce tilted crystals (towards the direction of the scanning order) and ultimately produce the observed contrast.

The tilting of the grains away from the build direction has been previously reported to depend on laser scan strategies [35–41]. For example, Thijs et al. [36] found that the elongated grains can be tilted 19° away from the build direction (towards the direction of the laser scan vector) when a uni-directional scan strategy is used for Ti-6Al-4V. Another observation from previous studies that it is relevant to highlight is the skewing of the crystallographic orientation away from the build direction observed by Carter et al. [34]. In that work, performed on a nickel superalloy produced with bi-directional scanning (analogous to the present study), some initial indications of displacement of the poles towards the direction of the scanning order were observed, although the effect was not fully characterized. In the two studies previously mentioned, the lack of a full-field imaging method – only EBSD was employed – made it impossible to characterize the extension of the areas displaying skewed grains with respect to the build direction. As it might be challenging to easily understand the contrast mechanisms form Figure 5 alone, we have included a step-by-step example in SI.

3.4. In-situ tensile test

Having established a good understanding about the diffraction contrast imaging signal and its interpretation in regard to the preferred grain orientation, we performed in-situ uni-axial tensile testing on a sample manufactured with the Z-scan strategy.

The texture evolution along the build direction ($\omega = 0°$) was studied with $\lambda = 3.8$ Å, through a tensile test with continuous deformation (10 μm/min), as illustrated in Fig. 6. An animated sequence can be found in the SI and the stress – deformation curve can be found in Fig. S5. The wavelength $\lambda = 3.8$ Å is used to probe the (111) family of planes. Small black lines can be seen running perpendicular to the z-axis, which correspond to the stripe overlaps seen in Fig. 2b (as white lines). The difference in transmission between these lines and the rest of the sample suggest a different average orientation of the (111) planes in the overlaps. Indeed, pole figures obtained with EBSD indicate a more 'random texture' in the overlap regions.

In Fig. 6, decreasing transmission is obtained at higher deformations around the necking region, suggesting grain rotation during the tensile test, with a reorientation of the <111> directions. Previous studies have reported that the deformation of steel and other fcc materials takes place through an increase of local intra-granular misorientation, which is promoted by deformation twinning [42]. For example, Sinha

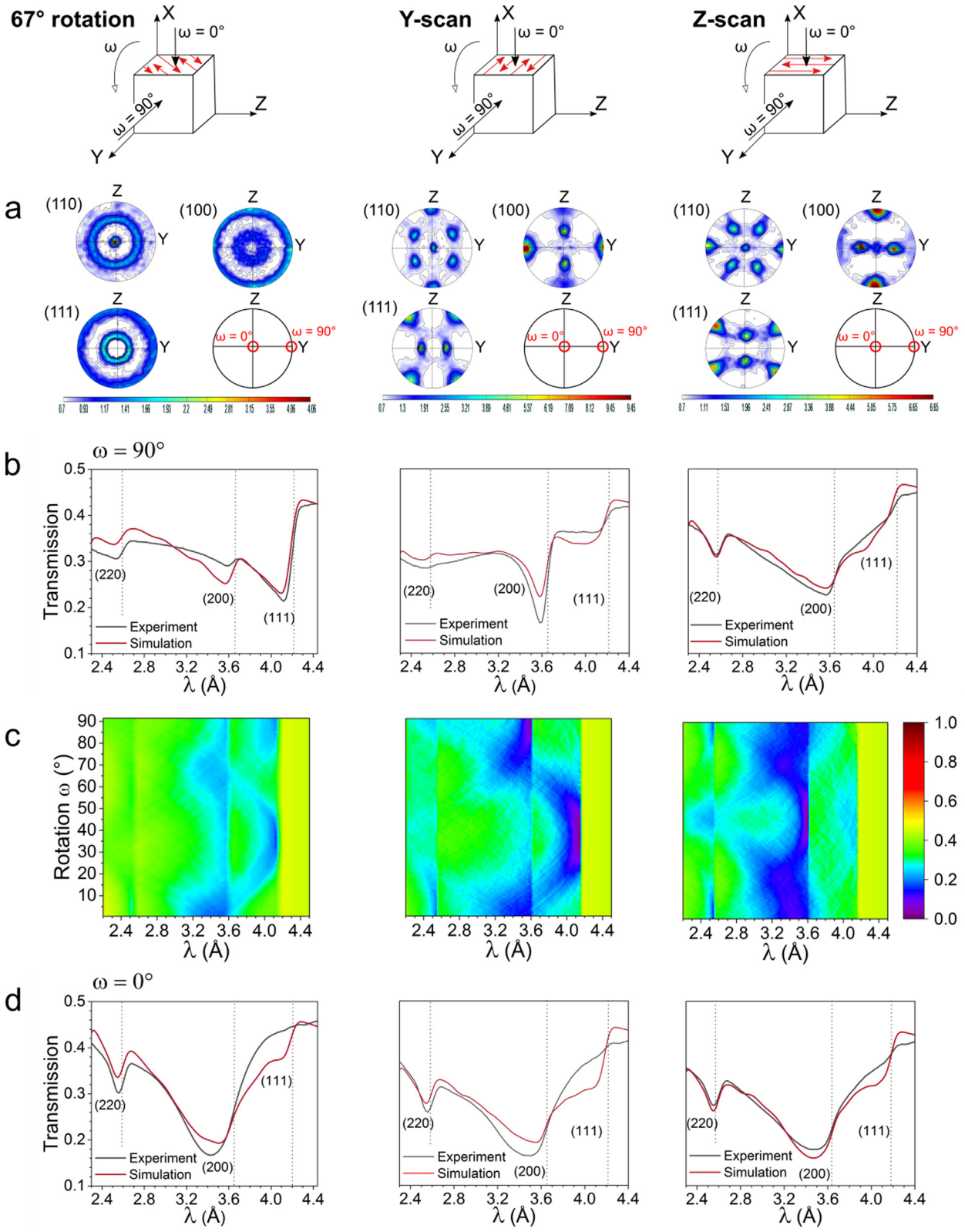

Fig. 4. a) Experimental neutron pole figures for the samples manufactured with the 67° rotation, Y-scan and Z-scan strategies. Adapted from [16]. b) Experimental (—) and simulated (—) Bragg-edge spectra at $\omega = 90°$ and d) $\omega = 0°$ (build direction aligned with neutron beam). In order to obtain an average description of the samples, the experimental transmission spectra were obtained from large areas of the specimens (see Fig. S4 of the SI), i.e. the 'bright/dark bands' are not separately considered in this case. c) Simulated transmission map for the sample rotations (ω) and different neutron wavelengths (λ).

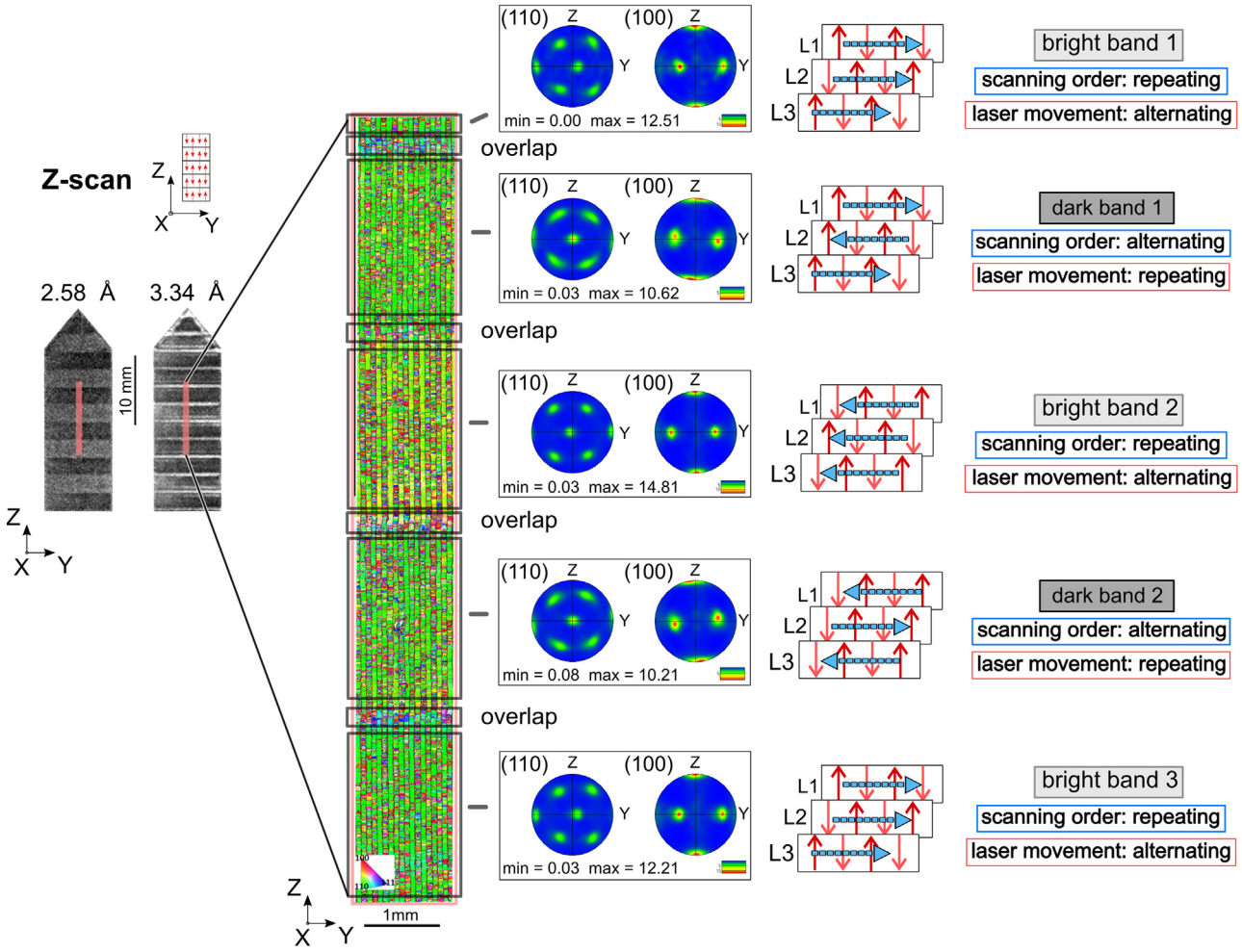

Fig. 5. Grain orientation map of a sample 'Z-scan' and the corresponding pole figures for the bands that are identified by diffraction contrast neutron imaging. An illustration of the Z-scan strategy is also included: the combination of scanning order direction (blue) and laser movement (red) result in four distinct bands (where bright band 3 equals bright band 1). The observed contrast in the neutron images can be explained by the pole figures.

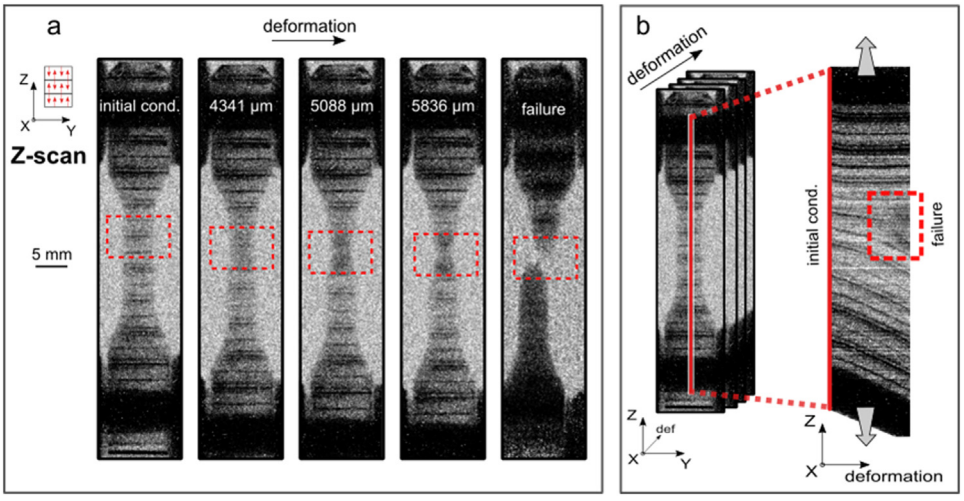

Fig. 6. a) Continuous deformation tensile test of a sample produced with the Z-scan strategy. Images taken at λ = 3.8 Å. The image (pixels) were normalized to an image collected at λ = 4.3 Å to highlight the contrast arising from neutron diffraction. The deformation (μm) at each step is indicated. Deformation rate = 10 μm/min. Neutron beam aligned with the x-axis, i.e. $\omega = 0°$. b) Visualizing the deformation of the cross section in one image by 're-slicing' the image stack, allowing to follow the failure evolution.

et al. [43] evaluated rolled 316L stainless steel with in-situ EBSD during tensile testing. They studied a cross-section that initially showed strong preferred orientation, with many grains having the normals of the (110) planes pointing out of observed cross-section (green in the EBSD color scheme). After fracture, a reduction of (110) grains was observed, with the simultaneous appearance of more grains oriented with the normals of the (111) planes pointing out of the cross-section (blue in the EBSD color scheme). These observations are in good agreement with our interpretation.

The location of the failure region during the continuous loading experiment can also be examined in Fig. 6. Notably, failure occurs by necking around one of the overlap regions, indicating that these areas of mi-

crostructural inhomogeneity could be sites where stresses concentrate. This suggests that the presence of the overlaps might be the limiting factor when it comes to the mechanical performance of parts manufactured with the stripe scan strategy, as these areas could represent weaker sections in the component.

The in-situ results are under further analysis and we intend to gain a better understanding of the grain rotation mechanism during deformation, by comparing the mechanical behaviour of the samples produced with the different laser scan strategies (Y, Z and rotation). Nonetheless, from this preliminary evaluation of the data, one can already draw valuable insights about the textural evolution and the nucleation sites for it. In particular, the time resolved in-situ imaging allows (by re-slicing of an image stack) to plot a cross section of the sample vs deformation stages (Fig. 6b), where the evolution can be followed even more clearly.

4. Conclusions

The preferential orientation that can be induced by different scan strategies in laser powder-bed fusion has been investigated through diffraction-based neutron imaging and large area EBSD mapping. The present study shows that even simple scan strategies, such as stripes with a displacement between the layers, can generate localized microstructural variations via the skewing of crystallographic orientations (observed in the bright bands). Furthermore, the movement of the laser controls the type, strength and sharpness of the texture at the local scale. Through in-situ experiments, it was found that grain rotation occurs during deformation of 316L, as evidenced by the observed reorientation of the <111> directions. We also demonstrated that failure of the Z-scan sample occurred by necking around one of the stripe overlaps, indicating that stresses concentrate in these areas. Therefore, it is suggested that the overlaps act as weakening spots to the detriment of the component's mechanical properties. This is a relevant factor that should be considered during the selection of scanning strategies (e.g. chess, stripes, islands, etc.) for enhanced mechanical performance. The fact that these observations can be revealed non-destructively by diffraction contrast neutron imaging, renders the technique very attractive for evaluating the microstructure and texture variations (across cm-length scales) that may arise due to the selection of different scan strategies in AM. We foresee the technique, when coupled with additional characterization and/or simulation tools as we demonstrated herein, to becoming a fundamental tool for understanding and evaluating texture evolution in AM and other novel fabrication techniques, thus enabling the development of functionalized anisotropic materials.

Data availability

The raw/processed data required to reproduce these findings cannot be shared at this time as the data also forms part of an ongoing study.

Declaration of Competing Interest

The authors declare that they have no known competing financial interests or personal relationships that could have appeared to influence the work reported in this paper.

Acknowledgements

This research is funded by the Swedish Foundation for Strategic Research (SSF) within the Swedish national graduate school in neutron scattering (SwedNess) and by the Swedish Foundation for Strategic Research (SSF), through the project "SSF – Development of processes and Materials in AM". This work was also supported by OP RDE MEYS, under the project "European Spallation Source – participation of the Czech Republic – OP", Reg. No. CZ.02.1.01/0.0/0.0/16013/0001794. Measurements were carried out at the CONRAD 2 instrument at Helmholtz-Zentrum Berlin für Materialien und Energie (HZB). The authors wish to thank Dr Ashok Menon, Dr Malcolm Guthrie and Dr Rebecca Clulow for proofreading our manuscript. The authors wish to thank Dr Alexandru A. Stoica for his guidance on the simulations. Dr Luc Dessieux acknowledges support at Oak Ridge National Laboratory from the US DOE Office of Scientific User facilities.

Supplementary materials

Supplementary material associated with this article can be found, in the online version, at doi:10.1016/j.mtla.2022.101614.

References

[1] S.A.M. Tofail, E.P. Koumoulos, A. Bandyopadhyay, S. Bose, L. O'Donoghue, C. Charitidis, Additive manufacturing: scientific and technological challenges, market uptake and opportunities, Mater. Today 21 (2018) 22–37, doi:10.1016/j.mattod.2017.07.001.

[2] A. Zhakeyev, P. Wang, L. Zhang, W. Shu, H. Wang, J. Xuan, Additive manufacturing: unlocking the evolution of energy materials, Adv. Sci. 4 (2017), doi:10.1002/advs.201700187.

[3] T.J. Horn, O.L.A. Harrysson, Overview of current additive manufacturing technologies and selected applications, Sci. Prog. 95 (2012) 255–282, doi:10.3184/003685012X13420984463047.

[4] J.O. Milewski, Additive Manufacturing of Metals, Springer International Publishing, Cham, 2017, doi:10.1007/978-3-319-58205-4.

[5] S.M. Thompson, L. Bian, N. Shamsaei, A. Yadollahi, An overview of direct laser deposition for additive manufacturing; Part I: transport phenomena, modeling and diagnostics, Addit. Manuf. 8 (2015) 36–62, doi:10.1016/j.addma.2015.07.001.

[6] P.Konda Gokuldoss, Design of next-generation alloys for additive manufacturing, Mater. Des. Process. Commun. 1 (2019) 19–22, doi:10.1002/mdp2.50.

[7] R. Petters, M. Stoica, S. Scudino, S. Pauly, L. Lo, Processing metallic glasses by selective laser melting, 16 (2013) 37–41. doi:10.1016/j.mattod.2013.01.018.

[8] M. Rafiee, R.D. Farahani, D. Therriault, Multi-material 3D and 4D printing: a survey, Adv. Sci. 7 (2020) 1–26, doi:10.1002/advs.201902307.

[9] M.S. Pham, B. Dovgyy, P.A. Hooper, C.M. Gourlay, A. Piglione, The role of side-branching in microstructure development in laser powder-bed fusion, Nat. Commun. 11 (2020) 1–12, doi:10.1038/s41467-020-14453-3.

[10] D.D. Gu, W. Meiners, K. Wissenbach, R. Poprawe, Laser additive manufacturing of metallic components: materials, processes and mechanisms, Int. Mater. Rev. 57 (2012) 133–164, doi:10.1179/1743280411Y.0000000014.

[11] K. Saeidi, D.L. Zapata, F. Lofaj, L. Kvetkova, J. Olsen, Z. Shen, F. Akhtar, Ultra-high strength martensitic 420 stainless steel with high ductility, Addit. Manuf. 29 (2019) 100803, doi:10.1016/j.addma.2019.100803.

[12] S. Pauly, L. Löber, R. Petters, M. Stoica, S. Scudino, U. Kühn, J. Eckert, Processing metallic glasses by selective laser melting, Mater. Today 16 (2013) 37–41, doi:10.1016/j.mattod.2013.01.018.

[13] V. Pacheco, D. Karlsson, J.J. Marattukalam, M. Stolpe, B. Hjörvarsson, U. Jansson, M. Sahlberg, Thermal stability and crystallization of a Zr-based metallic glass produced by suction casting and selective laser melting, J. Alloys Compd. 825 (2020) 153995, doi:10.1016/j.jallcom.2020.153995.

[14] J.J. Marattukalam, V. Pacheco, D. Karlsson, L. Riekehr, J. Lindwall, F. Forsberg, U. Jansson, M. Sahlberg, B. Hjörvarsson, Development of process parameters for selective laser melting of a Zr-based bulk metallic glass, Addit. Manuf. 33 (2020) 101124, doi:10.1016/j.addma.2020.101124.

[15] Z. Mahbooba, L. Thorsson, M. Unosson, P. Skoglund, H. West, T. Horn, C. Rock, E. Vogli, O. Harrysson, Additive manufacturing of an iron-based bulk metallic glass larger than the critical casting thickness, Appl. Mater. Today 11 (2018) 264–269, doi:10.1016/j.apmt.2018.02.011.

[16] J.J. Marattukalam, D. Karlsson, V. Pacheco, P. Beran, U. Wiklund, U. Jansson, B. Hjörvarsson, M. Sahlberg, The effect of laser scanning strategies on texture, mechanical properties, and site-specific grain orientation in selective laser melted 316L SS, Mater. Des. (2020) 193, doi:10.1016/j.matdes.2020.108852.

[17] P. Kürnsteiner, M.B. Wilms, A. Weisheit, B. Gault, E.A. Jägle, D. Raabe, High-strength Damascus steel by additive manufacturing, Nature 582 (2020) 515–519, doi:10.1038/s41586-020-2409-3.

[18] M. Garibaldi, I. Ashcroft, M. Simonelli, R. Hague, Metallurgy of high-silicon steel parts produced using Selective Laser Melting, Acta Mater. 110 (2016) 207–216, doi:10.1016/j.actamat.2016.03.037.

[19] T. Niendorf, S. Leuders, A. Riemer, H.A. Richard, T. Tröster, D. Schwarze, Highly anisotropic steel processed by selective laser melting, Metall. Mater. Trans. B Process Metall. Mater. Process. Sci. 44 (2013) 794–796, doi:10.1007/s11663-013-9875-z.

[20] R.R. Dehoff, M.M. Kirka, W.J. Sames, H. Bilheux, A.S. Tremsin, L.E. Lowe, S.S. Babu, Site specific control of crystallographic grain orientation through electron beam additive manufacturing, Mater. Sci. Technol. 31 (2015) 931–938, doi:10.1179/1743284714Y.0000000734.

[21] S. Hocine, H. Van Swygenhoven, S. Van Petegem, C.S.T. Chang, T. Maimaitiyili, G. Tinti, D. Ferreira Sanchez, D. Grolimund, N. Casati, Operando X-ray diffraction during laser 3D printing, Mater. Today 34 (2020) 30–40, doi:10.1016/j.mattod.2019.10.001.

[22] N. Nadammal, T. Mishurova, T. Fritsch, I.S. Muñoz, A. Kromm, C. Haberland, P.D. Portella, G. Bruno, Critical role of scan strategies on the development of microstructure, texture, and residual stresses during laser powder bed fusion additive manufacturing, Addit. Manuf. (2020) 101792, doi:10.1016/j.addma.2020.101792.

[23] A.M. Al-Falahat, N. Kardjilov, T.V. Khanh, H. Markötter, M. Boin, R. Woracek, F. Salvemini, F. Grazzi, A. Hilger, S.S. Alrwashdeh, J. Banhart, I. Manke, Energy-selective neutron imaging by exploiting wavelength gradients of double crystal monochromators—simulations and experiments, Nucl. Instrum. Methods Phys. Res. Sect. A Accel. Spectrometers, Detect. Assoc. Equip. 943 (2019) 162477, doi:10.1016/j.nima.2019.162477.

[24] R. Woracek, D. Penumadu, N. Kardjilov, A. Hilger, M. Strobl, R.C. Wimpory, I. Manke, J. Banhart, Neutron Bragg-edge-imaging for strain mapping under in situ tensile loading, J. Appl. Phys. 109 (2011) 1–5, doi:10.1063/1.3582138.

[25] B. Beausir, J.-J. Fundenberger, Analysis Tools for Electron and X-Ray Diffraction, ATEX - Software, Université de Lorraine, 2017.

[26] L.L. Dessieux, A.D. Stoica, P.R. Bingham, Single crystal to polycrystal neutron transmission simulation, Rev. Sci. Instrum. (2018) 89, doi:10.1063/1.5002102.

[27] R. Hielscher, H. Schaeben, A novel pole figure inversion method: specification of the MTEX algorithm, J. Appl. Crystallogr. 41 (2008) 1024–1037, doi:10.1107/S0021889808030112.

[28] V.F. Sears, Neutron scattering lengths and cross sections, Neutron news 3 (1992) 26–37.

[29] L.L. Dessieux, A.D. Stoica, P.R. Bingham, Ke An, M.J. Frost, H.Z. Bilheux, Neutron transmission simulation of texture in polycrystalline materials, Nuc. Inst. Meth. B (2019).

[30] C.Y. Ho, R.W. Powell, P.E. Liley, Thermal conductivity of the elements: a comprehensive review, J. Phys. Chem. Ref. Data 3 (supplement 1) (1974) I–1-I–796.

[31] T. Prohaska, J. Irrgeher, J. Benefield, J.K. Böhlke, L.A. Chesson, T.B. Coplen, J. Meija, Standard atomic weights of the elements 2021 (IUPAC Technical Report), Pure Appl. Chem. 94 (5) (2022) 573–600, doi:10.1515/pac-2019-0603.

[32] M. Busi, N. Kalentics, M. Morgano, S. Griffiths, A.S. Tremsin, T. Shinohara, R. Logé, C. Leinenbach, M. Strobl, Nondestructive characterization of laser powder bed fusion parts with neutron Bragg edge imaging, Addit. Manuf. 39 (2021) 101848, doi:10.1016/j.addma.2021.101848.

[33] R. Woracek, J. Santisteban, A. Fedrigo, M. Strobl, Diffraction in neutron imaging—a review, Nucl. Instrum. Methods Phys. Res. Sect. A Accel. Spectrometers, Detect. Assoc. Equip. 878 (2018) 141–158, doi:10.1016/j.nima.2017.07.040.

[34] L.N. Carter, C. Martin, P.J. Withers, M.M. Attallah, The influence of the laser scan strategy on grain structure and cracking behaviour in SLM powder-bed fabricated nickel superalloy, J. Alloys Compd. 615 (2014) 338–347, doi:10.1016/j.jallcom.2014.06.172.

[35] A. Leicht, C.H. Yu, V. Luzin, U. Klement, E. Hryha, Effect of scan rotation on the microstructure development and mechanical properties of 316L parts produced by laser powder bed fusion, Mater. Charact. 163 (2020) 110309, doi:10.1016/j.matchar.2020.110309.

[36] L. Thijs, F. Verhaeghe, T. Craeghs, J. Van Humbeeck, J.P. Kruth, A study of the microstructural evolution during selective laser melting of Ti-6Al-4V, Acta Mater. 58 (2010) 3303–3312, doi:10.1016/j.actamat.2010.02.004.

[37] P. Lamparter, S. Steeb, Structure of amorphous and molten alloys, Mater. Sci. Technol, Wiley-VCH Verlag GmbH & Co. KGaA, Weinheim, Germany, 2006, doi:10.1002/9783527603978.mst0004.

[38] H.L. Wei, J. Mazumder, T. DebRoy, Evolution of solidification texture during additive manufacturing, Sci. Rep. 5 (2015) 1–7, doi:10.1038/srep16446.

[39] A.R.A. Dezfoli, W.S. Hwang, W.C. Huang, T.W. Tsai, Determination and controlling of grain structure of metals after laser incidence: theoretical approach, Sci. Rep. 7 (2017) 1–11, doi:10.1038/srep41527.

[40] R. Shi, S.A. Khairallah, T.T. Roehling, T.W. Heo, J.T. McKeown, M.J. Matthews, Microstructural control in metal laser powder bed fusion additive manufacturing using laser beam shaping strategy, Acta Mater. 184 (2020) 284–305, doi:10.1016/j.actamat.2019.11.053.

[41] K.A. Sofinowski, S. Raman, X. Wang, B. Gaskey, M. Seita, Layer-wise engineering of grain orientation (LEGO) in Laser Powder Bed Fusion of stainless steel 316L, Addit. Manuf. (2020) 101809, doi:10.1016/j.addma.2020.101809.

[42] K. Yvell, T.M. Grehk, P. Hedström, A. Borgenstam, G. Engberg, EBSD analysis of surface and bulk microstructure evolution during interrupted tensile testing of a Fe-19Cr-12Ni alloy, Mater. Charact. 141 (2018) 8–18, doi:10.1016/j.matchar.2018.04.035.

[43] S. Sinha, J.A. Szpunar, N.A.P. Kiran Kumar, N.P. Gurao, Tensile deformation of 316L austenitic stainless steel using in-situ electron backscatter diffraction and crystal plasticity simulations, Mater. Sci. Eng. A 637 (2015) 48–55, doi:10.1016/j.msea.2015.04.005.